Poly(ethylene 2,5-furandicarboxylate) pole figures to determine the microstructural scheme upon uniaxial stretching: Link between orientation and crystallisation

Emilie Forestier, Christelle Combeaud, Nathanael Guigo, Nicolas Sbirrazzuoli, Gabriel Monge, Jean-Marc Haudin

Polymer 312 (2024) 127613

Contents lists available at ScienceDirect

Polymer

journal homepage: www.elsevier.com/locate/polymer

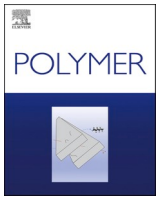

Poly(ethylene 2,5-furandicarboxylate) pole figures to determine the microstructural scheme upon uniaxial stretching: Link between orientation and crystallisation

Emilie Forestier [a,b,c], Christelle Combeaud [a,*], Nathanael Guigo [b], Nicolas Sbirrazzuoli [b], Gabriel Monge [a], Jean-Marc Haudin [a]

[a] Mines Paris, PSL University, Centre for Material Forming (CEMEF), UMR CNRS 7635, 06904, Sophia Antipolis, France
[b] Université Côte d'Azur, CNRS, Institut de Chimie de Nice (ICN), UMR 7272, 06108, Nice, Cedex 2, France
[c] Agence de l'Environnement et de la Maîtrise de l'Energie 20, avenue du Grésillé- BP 90406 49004 Angers, Cedex 01, France

ARTICLE INFO

Keywords:
Poly(ethylene 2,5-furandicarboxylate)
Pole figures
Crystalline orientation
Microstructural development
Strain-induced crystallisation (SIC)

ABSTRACT

The emergent biobased polymer poly (ethylene 2,5-furandicarboxylate), PEF, has been studied through an innovative approach based on pole figures and orientation factor calculation. PEF uniaxial stretching was performed with different mechanical conditions (different equivalent strain rates), up to several levels of strain and while considering different post-stretching cooling conditions (interrupted, unloaded and ruptured samples). Samples were stretched and interrupted before and after the Natural Draw Ratio (NDR), the deformation for which the material starts strain-hardening. When PEF strain-hardens, it reveals both an increase of the crystalline orientation and crystallinity ratio with the deformation imposed. Unloading the material at temperature tends to decrease partially crystalline orientation, especially regarding the aliphatic part of the chains. Moreover, stretching PEF up to high strains, superior to the NDR, leads to crystal fragmentation. After all, all experimental results were compared to a texture model. It appears that a texture can be developed upon stretching that is close to a fibre texture, as the furan cycles tend to be parallel to the specimen plane.

1. Introduction

Poly (ethylene 2,5-furandicarboxylate) is an emerging polyester resulting from the esterification of 2,5-furandicarboxylic acid (FDCA) and bio-ethylene glycol (EG). Over the last few years, this bio-based polymer, referred to as PEF, has proved to be a serious candidate for complementing, and in certain applications replacing, polyethylene terephthalate, or PET, regarding its interesting mechanical and thermal properties [1–8]. A non-exhaustive gathering of works dealing with PEF properties (mechanical, thermal and barrier) can be found thereafter [7, 9–33]. Just like PET and especially for food packaging applications, PEF, due to its ability in developing a crystalline texture, does present promising properties. PEF can even be more attractive than PET, as testified by its relevant thermal and barrier properties [34–36]. PET remains a petro-sourced polymer with thermal stability, good stiffness, relevant barrier properties and transparency. Today, Injection Stretch Blow Moulding (ISBM) or thermoforming processes rely obviously on all PET features.

Nowadays, more and more studies are also dealing with PEF end of life, as well as its future market implementation [37–41]. The presence of this promising polymer aims at being increased in the consumer daily life in the next years. PEF chain is composed of a furan cycle, with 4 carbons and one oxygen atoms, that leads to a hindered chain mobility [10]. The flip of the furan cycle is not easily authorized, contrary to the symmetrical benzene ring present in PET. Moreover, PEF furan cycle has two non-binding electrons contrary to PET. The flipping of PEF furan cycles does require much more energy, while PET benzene flips are facilitated. These differences in molecular structures, and thus chain mobilities, lead to new physical properties for PEF, such as a higher glass transition temperature and an apparent increased stiffness, a slower crystallisation kinetics in quiescent conditions and enhanced barrier properties [7,13,21].

Above their glass transition temperature, both amorphous PET and PEF present visco-hyperelastic behaviours. They can then accommodate large deformations involved by ISBM or thermoforming processes. Nevertheless, as the α-transition of PET and PEF are close but not

* Corresponding author.
E-mail address: christelle.combeaud@minesparis.psl.eu (C. Combeaud).

https://doi.org/10.1016/j.polymer.2024.127613
Received 10 June 2024; Received in revised form 6 September 2024; Accepted 7 September 2024
Available online 10 September 2024
0032-3861/

completely equivalent, the way they must be processed has to be understood and well-controlled. In Parallel to mechanical analysis, it appears also of prime interest to explore their ability in developing organised structures by Strain-Induced Crystallisation (SIC) upon uniaxial and biaxial stretchings. As reported elsewhere, developing SIC is clearly influenced by the stretching conditions of temperature, strain rate and cooling: a stable and textured microstructure will depend on the thermomechanical path imposed during the stretching [1–5,42–44]. By coupling mechanical analysis and microstructural development understanding, these studies have contributed to point out the main differences that can be observed between PEF and PET.

Relevant and controlled stretching conditions have been identified for both polymers so as to promote the development of organised and textured structures. PET is described as a polyester presenting a mesophase or "intermediate phase", whose local organisation definition strongly depends on the stretching and post-stretching conditions. For PEF, the scenario is slightly different as a well-organised microstructure can be directly observed just before and after the natural draw ratio (NDR), which is characterised by a strong strain-hardening of the material. Crystalline organisation continues to develop all along the hardening phase: the deformation plays an important role in promoting SIC [2,5,42]. As a matter of fact, this hardening can be explained by chains orientation and elongation, especially involving ethylene glycol and furan cycle conformation evolution from *gauche* to *trans* and *anti* to *syn*, respectively [35]. In a nutshell, upon stretching, PEF can develop crystalline phase that is equivalent to that obtained in quiescent conditions, and these structures do not seem to be strongly influenced by stretching conditions, contrary to PET. The key point is to consider PEF chain mobility while selecting the mechanical conditions. An approach based on master curves has been proven to be totally accurate [3,5]. Consequently, many mechanical conditions can lead to the development of a stable crystal.

As a matter of fact, to continue the comparison with PET, additional data is necessary especially a quantitative evaluation of the crystalline orientation (chain orientation, orientation of the furan cycles). Our first investigations concerning crystalline orientation in highly stretched PEF were based on Debye-Scherrer patterns and on the work of Mao et al. [1, 45,46]. However, it allows only a partial analysis of the sample orientation. In the present paper, the pole figure method is used, coupled with the calculation of orientation factors. This approach provides a much more complete description of this orientation and makes it possible to propose a model for the crystalline texture. Through pole figures the orientation degree due to processing can be quantified [47,48]. The results given by these sophisticated methods will be confronted to previous ones in order to propose a complete scenario for the microstructural development of PEF upon uniaxial stretching.

2. Material and methods

2.1. Material

Poly (ethylene 2,5-furandicarboxylate) was synthetised from direct esterification. To increase the molecular weight, a two-step process of melt-state followed by solid-state polycondensation of monoethylene glycol and 2,5-furandicarboxylic acid (FDCA) has been performed by Avantium Renewable Polymers. Amorphous extruded PEF sheets with a thickness of 700 μm were provided. The thickness of the stretched samples was around 300 μm. Samples were extracted in the extrusion direction to minimise thickness variation. Extrusions were performed according to the state of the art, after drying to avoid hydrolysis and degradation. Samples were stored under vacuum, in an aluminium-coated bag, in the freezer (−18 °C) to avoid water absorption and physical aging. Consequently, the polymer was tested dry as processed, without any pre-conditioning.

2.2. X-ray scattering

To analyse the organised phase, wide-angle X-ray scattering (WAXS) experiments were conducted on stretched specimens. For all the tests presented thereafter, uniaxially deformed flat films have been used. The stretching protocol used is described in Supporting Information (SI1) and has already been described largely elsewhere [1–3]. Stretched and air-quenched specimens were then in a second step analysed, in the processing zone of the samples.

2.2.1. Debye-Scherrer analysis and radial scans

2D Debye-Scherrer patterns using the flat-film camera technique under vacuum at ambient temperature were recorded. The sample-screen distance was set to 75 mm and the exposure time was kept constant at 45 min 1D scans, $I(2\theta)$, were also carried out at room temperature, in the transmission mode (from 10° to 50°), using a diffractometer Philips X'Pert PRO supplied by PANalytical. In both cases, the CuKα radiation ($\lambda_{CuK\alpha} = 1.54$ Å) was used. As experiments were performed in transmission, the scan intensities were normalised by the sample thickness.

2.2.2. The pole figure method and the calculation of orientation factors

a) Measurement and principle

Pole figures and orientation triangles were deduced from diffraction experiments using a diffractometer (Empyrean model PANalytical) equipped with an Eulerian cradle, with CuKα wavelength of 1.54 Å generated at a tension of 45 kV and an intensity of 30 mA.

The measurements were carried out by steps of 5° in reflection and in transmission, for an azimuthal angle ρ_z (angle between OZ and the normal to the diffracting plane, see Fig. 1a) ranging from 0° to 65° and from 60° to 90°, respectively.

The sample was rotated on 360° by steps of 5° for each ρ_z. A major problem is to superimpose transmission and reflection curves in the overlapping zone $\rho_z = 60°$ and $\rho_z = 65°$, to obtain the complete pole figure. Quantitatively, overlapping is expressed by Equation (1):

$$I(\rho_z, \beta_z) = I_{Texp}(\rho_z, \beta_z)R \quad (1)$$

I_{Texp} being the experimental intensity measured in transmission. In practice, we use an average value of R. Several choices are possible, which modifies more or less the pole figures, and finally the decision belongs to the operator.

Pole figures are stereographic projections, giving on a plane figure limited by a circle, the space distribution of the normals $\boldsymbol{N_{hkl}}$ to the {*hkl*} crystallographic planes. These projections are plotted in the OXYZ or (MD, TD, ND) frame of reference, where.

- OX = MD is the direction of longitudinal stretching, also called machine direction,

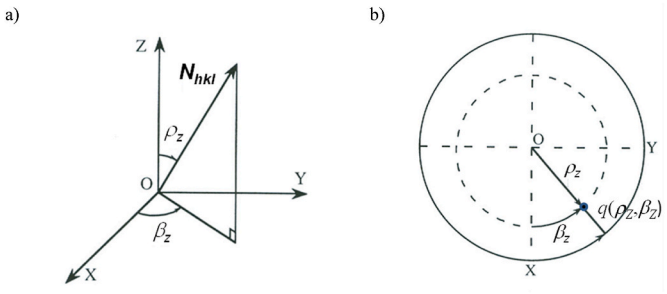

Fig. 1. (a) Characterisation of the orientation of a normal $\boldsymbol{N_{hkl}}$ in 3D-space by the couple (ρ_z, β_z); (b) Representation of the pole density q (ρ_z, β_z) on the stereographic projection.

- OY = TD is the transverse direction,
- OZ = ND is the direction of the film normal.

The film plane OXY or (MD, TD) is usually taken as projection plane. To construct a pole figure, the intensity diffracted by the {*hkl*} crystallographic planes is recorded as a function of two angles ρ_z (angle between OZ and the normal $\boldsymbol{N_{hkl}}$ to the diffracting plane), and β_z (angle between OX and the projection of $\boldsymbol{N_{hkl}}$ onto the OXY plane). These angles are visible in Fig. 1a. After corrections and normalisation, this intensity represents the density q (ρ_z, β_z) of $\boldsymbol{N_{hkl}}$ normals. A Wulff net graduated in ρ_z and β_z makes it possible to plot, for each couple (ρ_z, β_z), the value of q (ρ_z, β_z) on the stereographic projection (Fig. 1b). Isodensity lines are then drawn, the representative points being called poles. Level 1 corresponds to a density equal to the average density. These lines will be visible thereafter in the pole figures of the stretched samples.

Instead of the couple (ρ_z, β_z), the pole density can be represented in an equivalent way as a function of the couple (ρ_x, β_x): ρ_x is the angle between OX and $\boldsymbol{N_{hkl}}$, β_x is the angle between OY and the projection of $\boldsymbol{N_{hkl}}$ onto the (OYZ) plane (Fig. 2a). The couples (ρ_z, β_z) and (ρ_x, β_x) are compared on the stereographic projection in Fig. 2b.

b) Notion of orientation factors

Average state of crystalline orientation can be quantified by orientation factors, which are defined by the general equation:

$$f_{j,i} = \frac{3 < cos^2 \Phi_{j,i} > -1}{2} \tag{2}$$

where $< cos^2\ \Phi_{j,i} >$ represents the mean-square cosine of the angle $\Phi_{j,i}$ between a crystallographic axis $\boldsymbol{j}$ of the unit cell ($\boldsymbol{j} = \boldsymbol{a}, \boldsymbol{b}, \boldsymbol{c}$, with $\boldsymbol{c}$ the chain axis) and a macroscopic axis $\boldsymbol{i}$ ($\boldsymbol{i}$ = OX, OY, OZ = MD, TD, ND).

One has the following relations of orthogonality:

$$\sum_i < cos^2 \Phi_{j,i} > = < cos^2 \Phi_{j,MD} > + < cos^2 \Phi_{j,TD} > + < cos^2 \Phi_{j,ND} > = 1 \tag{3.a}$$

$$\sum_i f_{j,i} = f_{j,MD} + f_{j,TD} + f_{j,ND} = 0 \tag{3.b}$$

Table 1 gathers values of the orientation factors in special cases.

Fig. 3 depicts the Desper-Stein orientation triangle which geometrically represents through a point N inside a reference equilateral triangle the average orientation of axis $\boldsymbol{j}$ with respect to OXYZ (MD, TD, ND).

Equation 4.a to 4.c can be written as follows:

$$< cos^2 \Phi_{j,MD} > = \frac{NH}{ZR} \tag{4.a}$$

$$< cos^2 \Phi_{j,TD} > = \frac{NK}{ZR} \tag{4.b}$$

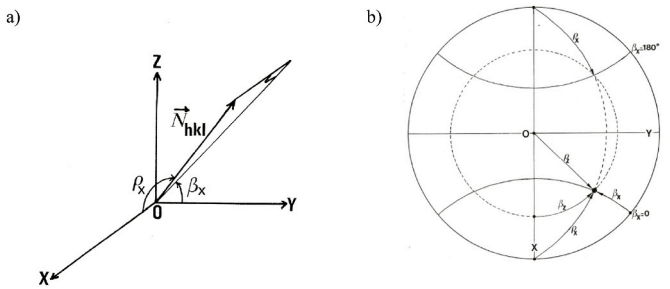

Fig. 2. (a) Characterisation of the orientation of $\boldsymbol{N_{hkl}}$ by the couple (ρ_x, β_x); (b) Representation of (ρ_z, β_z) and (ρ_x, β_x) on the stereographic projection.

Table 1
Typical values of orientation factors in special cases for given $\boldsymbol{i}$ and $\boldsymbol{j}$ values.

$< cos^2\ \Phi_{j,i} > = 1$ and $f_{j,i} = 1$	All the directions j are parallel to i
$< cos^2\ \Phi_{j,i} > = 0$ and $f_{j,i} = -\frac{1}{2}$	All the directions $\boldsymbol{j}$ are perpendicular to $\boldsymbol{i}$
$< cos^2\ \Phi_{j,i} > = \frac{1}{3}$ and $f_{j,i} = 0$	The directions $\boldsymbol{j}$ are distributed at random in 3D-space
$< cos^2\ \Phi_{j,i} > = \frac{1}{2}$ and $f_{j,i} = \frac{1}{4}$	The directions $\boldsymbol{j}$ are distributed at random in a plane containing $\boldsymbol{i}$

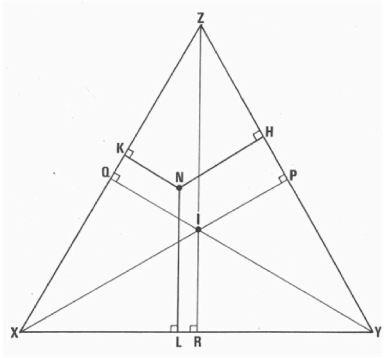

Fig. 3. The Desper-Stein orientation triangle [47].

$$< cos^2 \Phi_{j,ND} > = \frac{NL}{ZR} \tag{4.c}$$

with *NH, NK,* and *NL* the lengths of the perpendicular segments drawn from N to the different triangle sides.

This representation, due to Desper and Stein [47], verifies the orthogonality relation 3.a. Some particular situations are mentioned in Table 2.

c) Experimental determination of orientation factors

The experimental determination of orientation factors uses the pole densities q coming from different pole figures, and for a given *hkl* figure, the following quantities are calculated according to Equation (5).

$$< cos^2 \rho_{hkl,i} > = \frac{\int_0^{\frac{\pi}{2}} \int_0^{2\pi} q(\rho_i, \beta_i) cos^2(\rho_i) \sin(\rho_i) d\rho_i d\beta_i}{\int_0^{\frac{\pi}{2}} \int_0^{2\pi} q(\rho_i, \beta_i) \sin(\rho_i) d\rho_i d\beta_i} \tag{5}$$

This equation gives the average orientation of the normal $\boldsymbol{N_{hkl}}$, with $\boldsymbol{i}$ = OX, OY, OZ (X, Y, Z). The values of $< cos^2\ \Phi_{j,i} >$ are then deduced from geometrical calculations in the crystalline system of the polymer considered. We will present here the application of the general approach of Wilchinsky [48] to the monoclinic system, characteristic of the PEF

Table 2
Particular situations in the Desper-Stein triangle.

N in X	All the directions j are parallel to MD
N on YZ	All the directions $\boldsymbol{j}$ are perpendicular to MD
N on XP	Symmetry of revolution with respect to DM (uniaxial orientation of axis MD)
N in I	Isotropy

unit cell.

d) Application to the monoclinic system of PEF

The monoclinic unit cell of PEF was proposed by Mao et al. [45] and is defined by the vectors $\boldsymbol{a}$, $\boldsymbol{b}$ and $\boldsymbol{c}$, *i.e.*, by six parameters a, b, c, α, β, γ, with $\alpha = \beta = 90°$. One considers an orthogonal coordinate system ($\boldsymbol{A}$,$\boldsymbol{b}$, $\boldsymbol{c}$); $\boldsymbol{i}$, $\boldsymbol{j}$, $\boldsymbol{k}$ are the unit vectors carried by $\boldsymbol{A}$, $\boldsymbol{b}$, $\boldsymbol{c}$, respectively. Then, Equation 6.a to 6.e can be written.

$$\boldsymbol{A} = \boldsymbol{a}^* = \frac{\boldsymbol{b} \bigwedge \boldsymbol{c}}{V} \text{ vector of the reciprocal lattice} \tag{6.a}$$

$$V = (\boldsymbol{a}, \boldsymbol{b}, \boldsymbol{c}) = a * b * c * sin\gamma \tag{6.b}$$

$$\boldsymbol{i} = \boldsymbol{a}^* \, asin\, \gamma \tag{6.c}$$

$$\boldsymbol{j} = \frac{\boldsymbol{b}}{b} \tag{6.d}$$

$$\boldsymbol{k} = \frac{\boldsymbol{c}}{c} \tag{6.e}$$

We consider the average orientation of the normal $\boldsymbol{N_{hkl}}$ with respect to OZ. $\boldsymbol{n_{hkl}}$ (e,f,g) and $\boldsymbol{z}$ ($\cos\rho_A$, $\cos\rho_b$, $\cos\rho_c$) are the unit vectors carried by $\boldsymbol{N_{hkl}}$ and OZ, respectively. ρ_A, ρ_b, ρ_c, $\rho_{hkl,Z}$ are the angles between OZ and $\boldsymbol{A}$, $\boldsymbol{b}$ $\boldsymbol{c}$, $\boldsymbol{N_{hkl}}$, respectively. Then, while taking into account Equation (7) due to the symmetries of the monoclinic system, Equation 8.a and 8.b can be written:

$$< cos\,\rho_A\, cos\,\rho_c > = < cos\,\rho_b\, cos\,\rho_c > = 0 \tag{7}$$

$$cos\,\rho_{hkl,z} = \boldsymbol{n_{hkl}}.\boldsymbol{z} = e cos\rho_A + f cos\rho_b + g cos\rho_c \tag{8.a}$$

$$< cos^2\rho_{hkl,z} > = e^2 < cos^2\rho_A > + f^2 < cos^2\rho_b > + g^2 < cos^2\rho_c > + 2ef < cos\,\rho_A\, cos\,\rho_b > \tag{8.b}$$

In Equation 8.b, there are four unknowns <cos2 ρA>, <cos2 ρb>, <cos2 ρc>, <cos ρA cos ρb>, as e, f, g are supposed to be known. Additionally, <cos^2 $\rho_{hkl,z}$> is determined experimentally from *hkl* pole figure using Equation (5) with $\boldsymbol{i}$ = OZ (Z).

Therefore, 4 equations are needed: Equation 8.b for 3 different *hkl* pole figures (so, this equation appears three times) and Equation (9).

$$cos^2\rho_A + cos^2\rho_b + cos^2\rho_c = 1 \tag{9}$$

The solutions $< cos^2\rho_A >$, $< cos^2\rho_b >$ and $< cos^2\rho_c >$ of the system give access to the orientation factors f_A, f_b, f_c of $\boldsymbol{A}$, $\boldsymbol{b}$, $\boldsymbol{c}$ axes using Equation (2) with $\boldsymbol{j}$ = $\boldsymbol{A}$, $\boldsymbol{b}$, $\boldsymbol{c}$ and $\boldsymbol{i}$ = OZ (Z). The most interesting quantity is $< cos^2\rho_c >$, which characterizes the chain orientation in the crystalline phase. Then, Equation 10.a to 10.c and Equation (11) can be written:

$$e = d_{hkl}\left(\frac{h}{a\,sin\,\gamma} - \frac{k\,cos\,\gamma}{b sin\gamma}\right) \tag{10.a}$$

$$f = d_{hkl}\left(\frac{k}{b}\right) \tag{10.b}$$

$$g = d_{hkl}\left(\frac{l}{c}\right) \tag{10.c}$$

$$d_{hkl} = \frac{1}{\sqrt{\frac{h^2}{a^2 sin^2\gamma} + \frac{k^2}{b^2 sin^2\gamma} + \frac{l^2}{c^2} - \frac{2hkcos\gamma}{absin^2\gamma}}} \tag{11}$$

2.3. Differential scanning calorimetry (DSC)

DSC measurements were performed on a Mettler Toledo DSC 1 equipped with the STAR® software. Aluminium pans of 40 μL were used. Stretched samples are extremely thin, so the sample weight was about 1 mg. The enthalpy uncertainness is then evaluated at around 5 %.

To measure crystallinity ratios, the stretched samples were heated from 70 °C to 250 °C at a heating rate of 10 °C/min. Crystallinity ratios have been calculated according to Equation (12):

$$\chi_{SIC} = \frac{\Delta H_m - \Delta H_c}{\Delta H_m^0} \tag{12}$$

with χ_{SIC} the crystallinity ratio induced by the stretching, ΔH_m the melting enthalpy, ΔH_c the cold crystallisation enthalpy and ΔH_m^0 the equilibrium melting enthalpy, taken at 140 J g^{-1} for PEF as used elsewhere [13,18].

3. Results and discussion

3.1. Uniaxial stretching of PEF

In this paper, the crystal orientation is analysed through pole figures. However, as the samples were crystallised by strain-induced crystallisation (SIC), the mechanical behaviour of PEF must be briefly reminded thereafter to explain the differences observed within the samples microstructures. More references related to the mechanical behaviour of PEF can be found here [2–4,45,46].

Thus, to explain the microstructural orientation and crystallisation schemes, different stretching conditions have been selected. As mentioned in the stretching protocol (in Supporting Information), the influence of the chain mobility is explored through two different equivalent strain rates (10^{-1} s^{-1} and 10^{-2} s^{-1}), at a reference temperature of 100 °C. Fig. 4 shows the true stress-strain curves for these two equivalent strain rates.

As observed in Fig. 4, PEF uniaxial stretching in these conditions of strain rate and temperature leads to the development of an impressive strain hardening from a Natural Draw Ratio (NDR) that depends on the equivalent strain rate. The NDR appears for lower deformations as the equivalent strain rate is higher. It was reported that with an equivalent

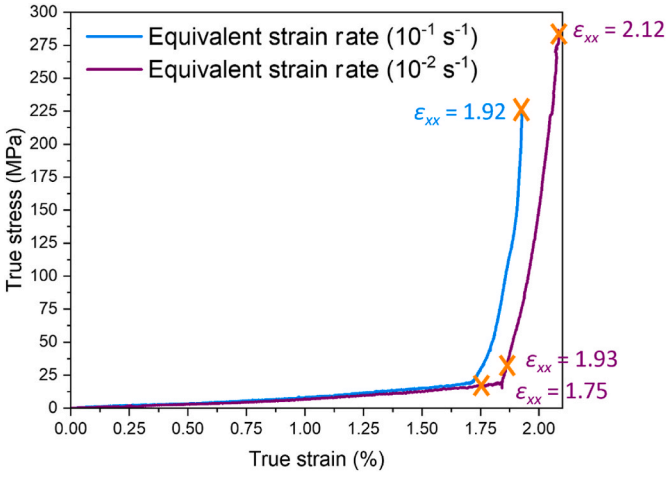

Fig. 4. True stress-strain curves of PEF upon uniaxial stretching for an equivalent strain rate of 10^{-1} s^{-1} (blue) and 10^{-2} s^{-1} (purple). The orange crosses represent the positions relative to the analysed samples: two "interrupted" positions during the stretching at 10^{-2} s^{-1} and two positions "at rupture", at the end of the stretching process. The strain level has been added for each mechanical condition following the colour code. (For interpretation of the references to colour in this figure legend, the reader is referred to the Web version of this article.)

strain rate of 10^{-2} s^{-1} (purple curve) the crystal of PEF exists even before the NDR, which means for a strain of 1.75 [2].

As a result, to understand the development of crystallinity upon uniaxial stretching, the crystallographic analyses have been performed on samples stretched at 10^{-2} s^{-1} up to a certain level of deformation, and then quenched with cold air to freeze the microstructure. Therefore, a first sample has been stretched in order to quantify the orientation before the NDR, until a deformation of 1.75 ($\varepsilon_{xx} = 1.75$). Two more samples, stretched for a deformation right after the NDR ($\varepsilon_{xx} = 1.93$) and until rupture have been selected to follow the evolution of the crystalline orientation with increasing strain. Additionally, another sample, labelled "unloaded", has been deformed and then unloaded at the same strain rate and temperature after stretching up to a deformation of 1.93 ($\varepsilon_{xx} = 1.93$, not represented in Fig. 4). This condition should highlight the influence of the cooling setting on crystalline orientation. Several cooling ways can exist during processing (quenching, unloading, annealing). Finally, a last specimen has been characterised until rupture and for an equivalent strain rate of 10^{-1} s^{-1}.

In a nutshell, five typical specimens have been chosen, labelled "interrupted $\varepsilon_{xx} = 1.75$", "interrupted $\varepsilon_{xx} = 1.93$", "unloaded $\varepsilon_{xx} = 1.93$", "rupture 10^{-2} s^{-1}" and "rupture 10^{-1} s^{-1}", respectively.

3.2. Analysis of the crystalline phase induced upon stretching

3.2.1. Debye-Scherrer patterns and radial scans

For all the specimens investigated, Debye-Scherrer patterns reveal a well-defined periodic organisation, i.e., crystallisation, through the existence of numerous diffraction spots. The same type of pattern was recorded just below and after the NDR, up to rupture, whatever the cooling conditions are, as already mentioned in other works [2]. A typical Debye-Scherrer pattern of stretched PEF is shown in Fig. 5. The distribution of diffraction spots suggests a uniaxial orientation of axis MD, commonly called fibre texture: the chain axes (***c*** axes) are parallel to MD and there is a symmetry of revolution with respect to MD. This assumption will be discussed further using pole figures and orientation factors.

The different diffraction spots were identified according to the monoclinic unit cell proposed by Mao et al. [45,46], which proves that only one crystalline phase is present.

Additional information is given by the radial scans of the diffracted intensity in the transverse direction, where three intense diffraction spots were identified in Fig. 5: $(\bar{1}10)$, (110) and (020).

Two types of curves are observed in Fig. 6. For the interrupted and unloaded tests the three peaks are well separated. For interrupted tests, an improvement of the crystalline organisation is observed qualitatively, when strain increases from 1.75 (just before NDR) to 1.93 (after NDR): the peaks become better defined and higher. Furthermore, the level of improvement is lower in the unloaded specimen than in the interrupted one at the same strain $\varepsilon_{xx} = 1.93$. The main differences are observable on the (020) planes.

For the two samples stretched up to the rupture, one observes one bump and the (020) peak. The bump is the result of the merging of the two first peaks due to the crystal fragmentation during solid-state deformation upon stretching [5,34]. Therefore, in a first step crystals are formed by SIC, and then the formed crystals undergo plastic deformation up to rupture.

3.2.2. Crystallinity ratio

Fig. 7 represents the crystallinity ratio associated to all the analysed samples.

At first glance, the crystallinity ratio is linked to the level of strain reached but is also slightly sensitive to the equivalent strain rate chosen. More in depth, things could be more complicated. In interrupted tests, the crystallinity ratio is about the same for $\varepsilon_{xx} = 1.75$ (27 %) and $\varepsilon_{xx} = 1.93$ (28 %). For the same strain $\varepsilon_{xx} = 1.93$, there is a great difference in crystallinity between the interrupted sample (28 %) and the unloaded sample (35 %), which shows the importance of cooling conditions. For the two samples at rupture, the crystallinity ratios are close (33 vs. 35 %), and close to the crystallinity of the sample unloaded (35 %). Finally, the results can be distributed into two families: on one hand the two samples "interrupted", and, on the other hand, the sample "unloaded" and the two samples "rupture". This conclusion is confirmed by the fact that a rupture can act just like a very rapid unloading in temperature, where the cooling is not well-controlled.

3.2.3. Pole figures and orientation factors

Because of the geometry of the diffraction experiment, a Debye-Scherrer pattern gives only a partial representation of the sample orientation. The pole figure method coupled with the calculation of orientation factors provides a much more complete description of this orientation. In supporting information, the interest of pole figures with

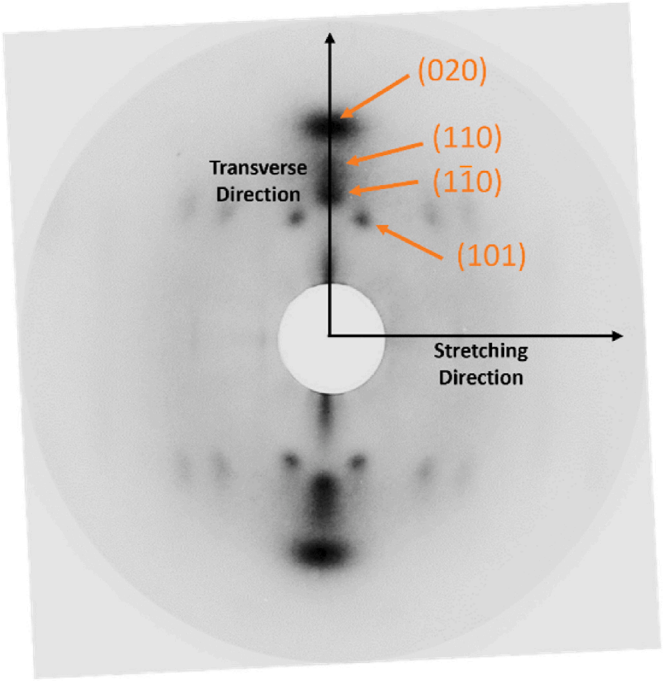

Fig. 5. Typical Debye-Scherrer pattern of the stretched samples.

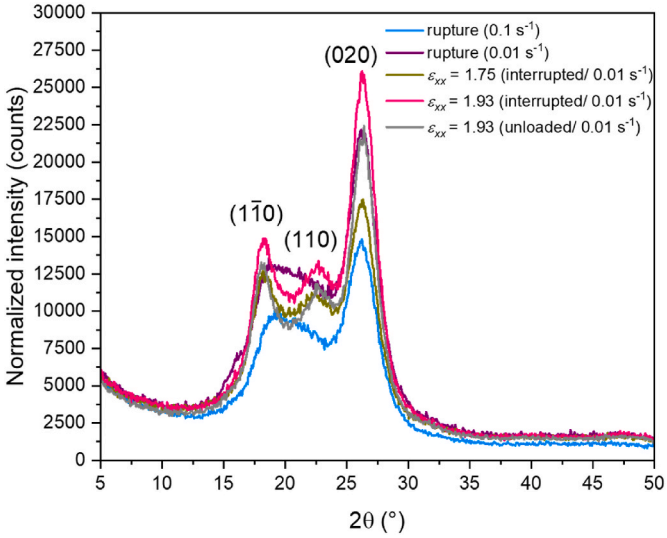

Fig. 6. Radial scans in the transverse direction of all the analysed samples.

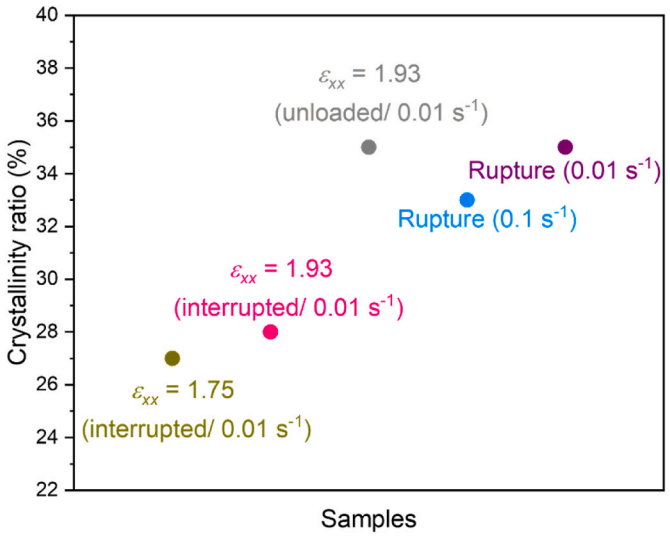

Fig. 7. Evolution of the crystallinity ratio for the studied samples.

respect of Debye-Scherrer diagrams is presented.

After several attempts, only two reflections, (020) and (101) (see Fig. 5), were available to plot pole figures. This means that one *hkl* reflection is missing for the application of Wilchinsky's method presented in Section 2.2.2.d. Consequently, we supposed that $< \cos \rho_A \cos \rho_b > \approx 0$, which seems reasonable since the angle γ is close to 90° ($\gamma = 103.3°$).

The pole F igs. 101 and 020 are shown in Figs. 8 and 9, respectively. To allow an easy comparison of the levels of orientation, we have also indicated in Fig. 10, for each condition, the values of $< cos^2\rho_{c,OX} >$ and $< cos^2\rho_{b,OZ} >$, calculated according to the procedures given in Section 2.2.2.

The 101 pole figures consist of four lobes, which are more or less well-defined (Fig. 8). The 020 pole figures give the distribution of the normal to the (020) planes, which are the planes containing the furan cycles [46]. The poles are located in a band perpendicular to the stretching direction MD (Fig. 9), without symmetry of revolution around MD, since the highest pole densities are concentrated around the centre of the figure. This shows that.

- the texture is close to a fibre texture but is not a pure fibre texture, as it could have been suggested by the Debye-Scherrer patterns;
- the furan rings tend to be parallel to the film surface.

This important result justifies in itself the use of pole figures, since it gives access to features of the texture, which were not available with Debye-Scherrer patterns.

The average orientation of crystalline chains is quantified by $< cos^2\rho_{c,OX} >$ (Fig. 10a). It appears that:

- For *interrupted tests*, when strain passes from 1.75 to 1.93, an increase of orientation is observed, $< cos^2\rho_{c,OX} >$ passing from 0.68 to 0.91.
- $< cos^2\rho_{c,OX} >$ reaches its lowest value (0.67) with the *unloaded specimen*. The 101 pole figure appears to be less defined, with the four lobes almost disappearing. The unloading step seems to have less influence on the 020 pole figure. These results could show a slight disorientation during the unloading process, associated with some relaxation of the crystalline orientation.
- The case of the tests *to rupture* is more complicated. On one side, the test performed up to rupture with an equivalent strain rate of 10^{-1} s^{-1} gives the highest orientation level ($< cos^2\rho_{c,OX} > = 0.94$), right before the specimen interrupted at $\varepsilon_{xx} = 1.93$ ($< cos^2\rho_{c,OX} > = 0.91$) with an equivalent strain rate of 10^{-2} s^{-1}. Both specimens were stretched at two different strain rates up to about the same strain (1.92 vs. 1.93), which induced different microstructures: in the specimen at rupture, crystals have already undergone fragmentation, while in the interrupted one, they have not yet. Therefore, it could be thought that the level of strain reached is determinant in the chain orientation. On the other side, for the test performed up to rupture at 10^{-2} s^{-1}, $< cos^2\rho_{c,OX} >$ reaches a value close to the one of the interrupted test at $\varepsilon_{xx} = 1.75$ ($< cos^2\rho_{c,OX} > = 0.69$). However, this

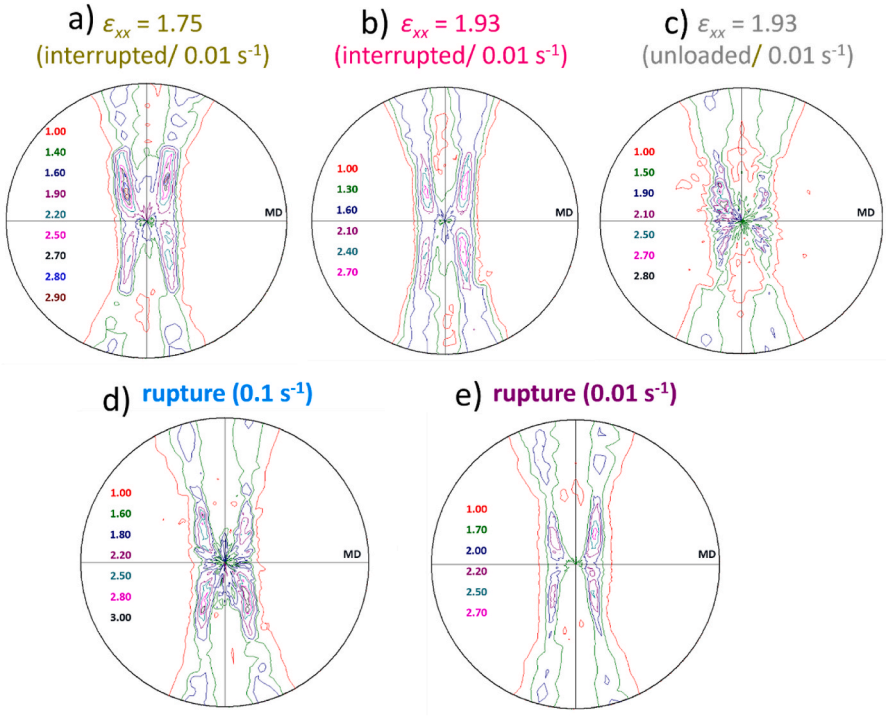

Fig. 8. Crystallographic texture developed in the samples for the plane (101).

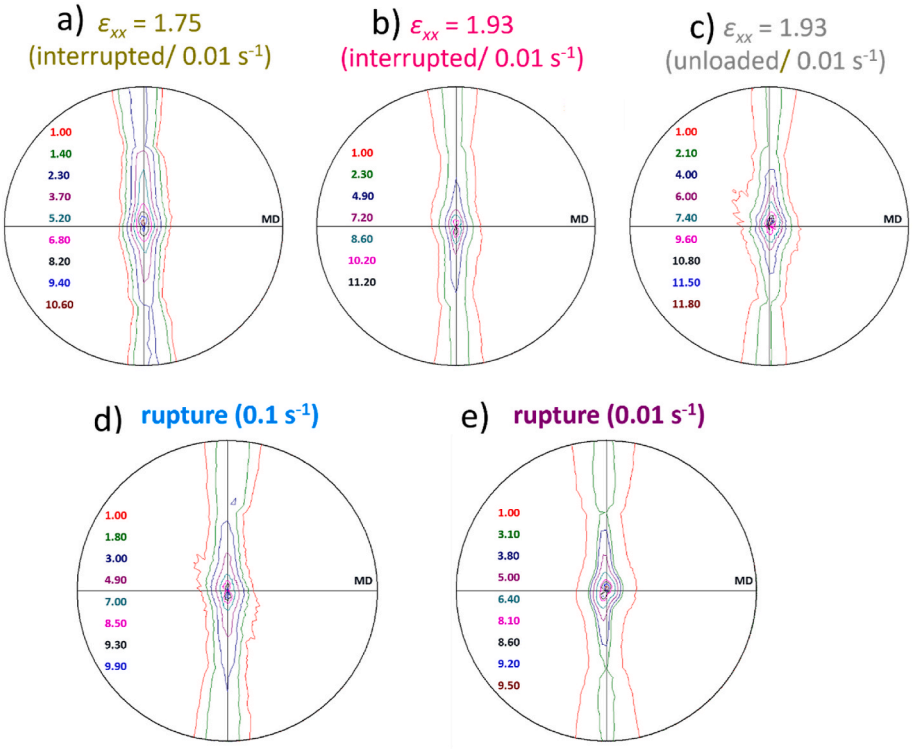

Fig. 9. Crystallographic texture developed in the samples for the plane (020).

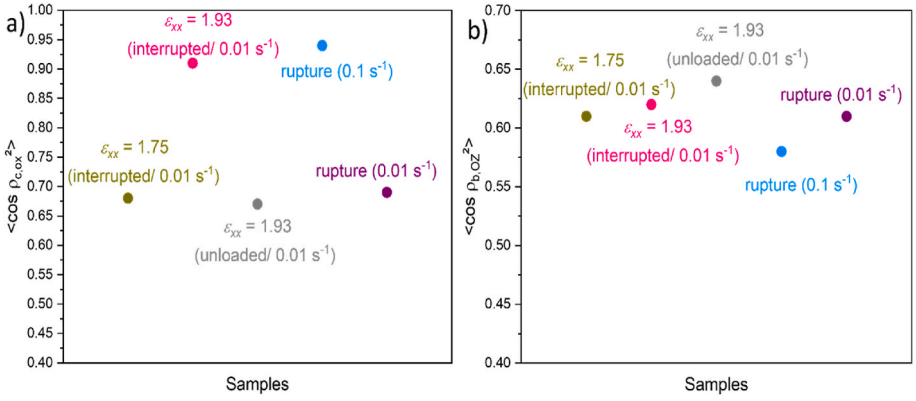

Fig. 10. Evolution of (a) $< cos^2\rho_{c,OX} >$ and (b) $< cos^2\rho_{b,OZ} >$.

specimen was stretched up to $\varepsilon_{xx} = 2.12$. The comparison of the results from both sides shows that the role of the level of strain reached is not so obvious. Indeed, the specimens "rupture" underwent a series of events: SIC, plastic deformation, rupture and brutal unloading. SIC and plastic deformation increase crystalline orientation. Rupture and unloading partly relax this orientation.

The mean orientation of the normals $\boldsymbol{N_{020}}$ to the (020) planes with respect to the OZ-axis is described by $< cos^2\rho_{020,OZ} >$ which, in the monoclinic system of PEF, is different from $< cos^2\rho_{b,OZ} >$. The two quantities are related by Equation 8.b but, as we assume here that γ is close to 90°, we can equate them and use $< cos^2\rho_{b,OZ} >$ to describe the mean orientation of the normals $\boldsymbol{N_{020}}$, and consequently the mean orientation of the (020) planes. Experimentally, the values of $< cos^2\rho_{b,OZ} >$ range from 0.58 to 0.64 and will be analysed in the following section using a model of texture. It is difficult to correlate them to experimental conditions. Nevertheless, the highest value corresponds to the unloaded specimen, which has the lowest chain orientation. Conversely, the lowest value of $< cos^2\rho_{b,OZ} >$ corresponds to the highly oriented rupture (10^{-1} s^{-1}) specimen (See Fig. 10a and 10b).

3.3. Models of texture

According to the previous results, it appears that the sample stretched up to a strain of 1.93 and interrupted has developed a well-defined crystallographic texture. Fig. 11 depicts the Desper-Stein orientation triangle.

To interpret this figure, several models can be proposed as shown in Fig. 12, Tables 3 and 4.

- The fibre-texture model, as suggested by the Debye-Scherrer pattern (Fig. 5);
- A model where all the chain axes are in the machine direction and all the furan rings are in the specimen plane, suggested by maximum intensities at the centre of the 020 pole figure.

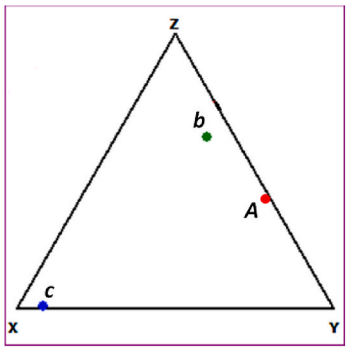

Fig. 11. Desper-Stein orientation triangle for the sample stretched up to a strain of 1.93 and interrupted.

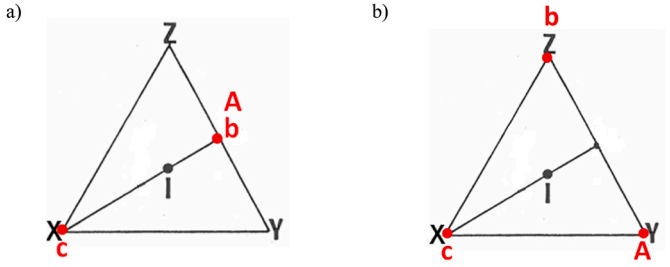

Fig. 12. (a) Model of fibre texture and (b) Model of texture with all the furan rings in the specimen plane.

Table 3
Values of the $< cos^2\Phi_{j,i} >$ for the fibre texture.

	A	B	C
$< cos^2\Phi_{j,OX} >$	0	0	1
$< cos^2\Phi_{j,OY} >$	0.5	0.5	0
$< cos^2\Phi_{j,OZ} >$	0.5	0.5	0

Table 4
Values of the $< cos^2\Phi_{j,i} >$ for the texture with all the furan rings in the specimen plane.

	A	B	C
$< cos^2\Phi_{j,OX} >$	0	0	1
$< cos^2\Phi_{j,OY} >$	1	0	0
$< cos^2\Phi_{j,OZ} >$	0	1	0

Fig. 12, Tables 3 and 4 have been established from the guidelines given in Section 2.2.2.

The comparison between the models and the actual texture shows that.

- The texture is not too far from a fibre texture, but with an important deviation since ***A*** and ***b*** are not located on the median of the orientation triangle;
- The displacement of ***b*** toward Z indicates the trend of the furan cycles to be located in the specimen plane. This trend can be appreciated by the value of $< cos^2\rho_{b,OZ} >$. It is 0.5 for a pure fibre texture and 1 when all the furan rings are in the specimen plane.

Therefore, we propose an intermediate model with the value x assigned to $< cos^2\rho_{b,OZ} >$ (Fig. 13 and Table 5).

The model for x equal to the experimental value $x = 0.62$ is in good agreement with the experimental texture (Table 6 and comparison of Figs. 11 and 13). The small differences observed result from the fact that ***c*** is not exactly in X, which brings ***b*** and ***A*** slightly inside the triangle.

The intermediate model, which was quantitatively established in a particular case, is valid for all the investigated specimens and makes it possible to interpret values of $< cos^2\rho_{b,OZ} >$ between 0.5 and 1.

3.4. Discussion

Strain-Induced Crystallisation of PEF begins just before the NDR [2]. The crystalline texture developed is not a pure fibre texture since the furan cycles tend to be parallel to the specimen plane. This trend remains moderate because the flip of the furan ring is not easily authorized contrary to the benzene ring in PET [37,43].

In a strain range from before the NDR to beyond the NDR, typically from 1.75 to 1.93 for an equivalent strain rate of 10^{-2} s^{-1}, the main result is an increase of crystalline orientation in the interrupted tests. In this strain range, the main phenomenon is probably a perfection of SIC, and perhaps there is an onset of plastic deformation of the crystals formed, without crystal fragmentation (no overlapping of $(\overline{110})$ and (110) reflections). According to present results as well as previous ones [5], crystal fragmentation should occur for a strain about 2.00 in the case of a strain rate of $10-^{2}$ s^{-1}.

The role of the unloading procedure can be understood through the comparison of the specimens interrupted and unloaded that have been stretched with an equivalent strain rate of 10^{-2} s^{-1}, up to $\varepsilon_{xx} = 1.93$. Unloading introduces some relaxation phenomenon: the orientation of crystalline chains decreases while crystallinity ratio increases. Finally, the furan cycles are better oriented parallel to the specimen plane in the unloaded specimen. As a reminder, furan cycles alignment does require conformational changes from *anti* to *syn* which are complex and energy consuming: the cycle remains also asymmetric due to the presence of an oxygen atom. The unloading path in temperature which can act as an annealing step can authorise local perfection of the furan rings packing that was not completely achieved. Intermolecular interactions (furan cycle/furan cycle) could then be optimised in the pre-organised domains that were not totally stabilised. On the contrary, the aliphatic part of the chains can be considered as more "fragile segments" in their extended or "over-extended" *trans* conformation as intermolecular interactions are weaker. Relaxation phenomenon could rather play an important role on the disorientation of these regions that appear far less oriented with the unloading path. This is in agreement with the fact that these disorientations can promote crystalline perfections elsewhere, especially the furan cycle alignments, enhancing the global crystallinity of the material.

Understanding the orientation in specimens at rupture is not so easy,

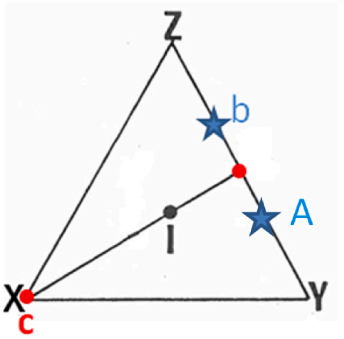

Fig. 13. Intermediate texture between the fibre texture and the model with all the furan rings in the specimen plane.

Table 5
Values of the $< cos^2\Phi_{j,i} >$ for the intermediate texture.

	A	b	C
$< cos^2\Phi_{j,OX} >$	0	0	1
$< cos^2\Phi_{j,OY} >$	x	1-x	0
$< cos^2\Phi_{j,OZ} >$	1-x	0.5 $< x <$ 1	0

Table 6
Values of the $< cos^2\Phi_{j,i} >$ for the intermediate texture for $x = 0.62$ (in red). Comparison with the experimental values in black.

	A	b	C
$< cos^2\Phi_{j,OX} >$	0.01	0.08	0.91
	0	0	1
$< cos^2\Phi_{j,OY} >$	0.62	0.30	0.08
	0.62	0.38	0
$< cos^2\Phi_{j,OZ} >$	0.37	0.62	0.01
	0.38	0.62	0

since these specimens have undergone a complex history: SIC, plastic deformation with crystal fragmentation, rupture and unloading. The crystalline orientation can be high (like in rupture 10^{-1} s^{-1}) or relatively weak (like in rupture 10^{-2} s^{-1}), which is perhaps related to the value of the stretching temperature: 98 °C (10^{-1} s^{-1}) vs. 105 °C (10^{-2} s^{-1}). A higher stretching temperature favours chain relaxation, which leads to a lower chain orientation. Their crystallinity is close to that of the unloaded specimen, which suggests that some relaxation has occurred as in the unloaded specimen.

4. Conclusion

To conclude, this work has shown that coupling WAXS measurements with texture analysis allows us to go deeper in the understanding of SIC development scenarios of PEF upon stretching. Indeed, PEF can develop in its rubbery-like state Strain-Induced Crystallisation (SIC) whose orientation clearly depends on the parameter settings of the stretching protocol: level of strain and cooling conditions such as unloading, quenching or rupture of the specimen. As expected, crystallinity development is enhanced with the deformation imposed as the amount and perfection of the crystalline phase increase. In parallel, crystalline phase is getting more and more oriented. Moreover, compared to the quenching, the unloading path in temperature, acting as an annealing step, leads to both an increase of crystalline domains (possible perfection of organised parts) and to an obvious loss of crystalline orientation. In fact, relaxation phenomenon localised along the aliphatic part of the chain may authorise some crystalline perfectioning elsewhere, which is consistent with the increase of crystallinity ratio. After all, a proposal of a model of texture is presented and discussed. It highlights the fact that the texture observed is not far from the fibre texture. PEF furan rings tend to be efficiently aligned in the specimen plane, which is optimal for enhancement of barrier properties required for food packaging applications.

CRediT authorship contribution statement

Emilie Forestier: Writing – review & editing, Writing – original draft, Methodology, Investigation, Conceptualization. **Christelle Combeaud:** Writing – review & editing, Supervision, Funding acquisition, Conceptualization. **Nathanael Guigo:** Writing – review & editing, Supervision, Funding acquisition, Conceptualization. **Nicolas Sbirrazzuoli:** Writing – review & editing, Supervision, Funding acquisition, Conceptualization. **Gabriel Monge:** Methodology, Investigation. **Jean-Marc Haudin:** Writing – review & editing, Writing – original draft, Methodology, Investigation, Conceptualization.

Declaration of competing interest

The authors declare that they have no known competing financial interests or personal relationships that could have appeared to influence the work reported in this paper.

Data availability

No data was used for the research described in the article.

Acknowledgments

This work was supported by the French Environment and Energy Management Agency (ADEME), Sidel Group as well as Avantium Renewable Polymers.

Appendix A. Supplementary data

Supplementary data to this article can be found online at https://doi.org/10.1016/j.polymer.2024.127613.

References

[1] E. Forestier, C. Combeaud, N. Guigo, G. Monge, J.M. Haudin, N. Sbirrazzuoli, N. Billon, Strain-induced crystallization of poly(ethylene 2,5-furandicarboxylate). Mechanical and crystallographic analysis, Polymer 187 (2020), https://doi.org/10.1016/j.polymer.2019.122126.
[2] E. Forestier, C. Combeaud, N. Guigo, N. Sbirrazzuoli, N. Billon, Understanding of strain-induced crystallization developments scenarios for polyesters: comparison of poly(ethylene furanoate), PEF, and poly(ethylene terephthalate), PET, Polymer (Guildf) 203 (2020) 122755, https://doi.org/10.1016/j.polymer.2020.122755.
[3] E. Forestier, C. Combeaud, N. Guigo, G. Corvec, C. Pradille, N. Sbirrazzuoli, N. Billon, Comparative analysis of the mechanical behaviour of PEF and PET uniaxial stretching based on the time/temperature superposition principle, Polymers 13 (2021) 3295, https://doi.org/10.3390/POLYM13193295, 3295 13 (2021.
[4] G. Stoclet, J.M. Lefebvre, B. Yeniad, G. Gobius du Sart, S. de Vos, On the strain-induced structural evolution of Poly(ethylene-2,5-furanoate) upon uniaxial stretching: an in-situ SAXS-WAXS study, Polymer 134 (2018) 227–241, https://doi.org/10.1016/j.polymer.2017.11.071.
[5] E. Forestier, C. Combeaud, N. Guigo, N. Sbirrazzuoli, A proposal for enhanced microstructural development of Poly(ethylene 2,5-furandicarboxylate), PEF, upon stretching: on strain-induced crystallization and amorphous phase stability improvement, Polymer 246 (2022) 124775, https://doi.org/10.1016/J.POLYMER.2022.124775.
[6] A. Gandini, A.J.D. Silvestre, C.P. Neto, A.F. Sousa, M. Gomes, The furan counterpart of polyethylene terephthalate: an alternative material based on renewable resources, J. Polym. Sci. Polym. Chem. 47 (2009) 295–298, https://doi.org/10.1002/pola.23130.
[7] R.J.I. Knoop, W. Vogelzang, J. van Haveren, D.S. van Es, High molecular weight poly(ethylene-2,5-furanoate); critical aspects in synthesis and mechanical property determination, J. Polym. Sci. Polym. Chem. 51 (2013) 4191–4199, https://doi.org/10.1002/pola.26833.
[8] A. Bourdet, A. Esposito, S. Thiyagarajan, L. Delbreilh, F. Affouard, R.J.I. Knoop, E. Dargent, Molecular mobility in amorphous biobased poly(ethylene 2,5-furandicarboxylate) and poly(ethylene 2,4-furandicarboxylate), Macromolecules 51 (2018) 1937–1945, https://doi.org/10.1021/acs.macromol.8b00108.
[9] M.C. Righetti, M. Vannini, A. Celli, D. Cangialosi, C. Marega, Bio-based semi-crystalline PEF: temperature dependence of the constrained amorphous interphase and amorphous chain mobility in relation to crystallization, Polymer 247 (2022) 124771, https://doi.org/10.1016/J.POLYMER.2022.124771.
[10] S.K. Burgess, J.E. Leisen, B.E. Kraftschik, C.R. Mubarak, R.M. Kriegel, W.J. Koros, Chain mobility, thermal, and mechanical properties of poly(ethylene furanoate) compared to poly(ethylene terephthalate), Macromolecules 47 (2014) 1383–1391, https://doi.org/10.1021/ma5000199.
[11] G.Z. Papageorgiou, D.G. Papageorgiou, Z. Terzopoulou, D.N. Bikiaris, Production of bio-based 2,5-furan dicarboxylate polyesters: recent progress and critical aspects in their synthesis and thermal properties, Eur. Polym. J. 83 (2016) 202–229, https://doi.org/10.1016/j.eurpolymj.2016.08.004.
[12] V. Tsanaktsis, D.G. Papageorgiou, S. Exarhopoulos, D.N. Bikiaris, G. Z. Papageorgiou, Crystallization and polymorphism of poly(ethylene furanoate), Cryst. Growth Des. 15 (2015) 5505–5512, https://doi.org/10.1021/acs.cgd.5b01136.
[13] G.Z. Papageorgiou, V. Tsanaktsis, D.N. Bikiaris, Synthesis of poly(ethylene furandicarboxylate) polyester using monomers derived from renewable resources:

thermal behavior comparison with PET and PEN, Phys. Chem. Chem. Phys. 16 (2014) 7946–7958, https://doi.org/10.1039/c4cp00518j.
[14] T. Dimitriadis, D.N. Bikiaris, G.Z. Papageorgiou, G. Floudas, Molecular dynamics of poly(ethylene-2,5-furanoate) (PEF) as a function of the degree of crystallinity by dielectric spectroscopy and calorimetry, Macromol. Chem. Phys. 217 (2016) 2056–2062, https://doi.org/10.1002/macp.201600278.
[15] G.Z. Papageorgiou, G.N. Nikolaidis, R.O. Ioannidis, K. Rinis, D.G. Papageorgiou, P. A. Klonos, D.S. Achilias, M. Kapnisti, Z. Terzopoulou, D.N. Bikiaris, A step forward in thermoplastic polyesters: understanding the crystallization and melting of biobased poly(ethylene 2,5-furandicarboxylate) (PEF), ACS Sustain. Chem. Eng. (2022), https://doi.org/10.1021/ACSSUSCHEMENG.2C00995.
[16] L. Maini, M. Gigli, M. Gazzano, N. Lotti, D. Bikiaris, G. Papageorgiou, Structural investigation of poly(ethylene furanoate) polymorphs, Polymers 10 (2018) 296, https://doi.org/10.3390/polym10030296.
[17] G. Stoclet, A. Arias, B. Yeniad, S. De Vos, Relationships between crystalline structure and the thermal behavior of poly(ethylene 2,5-furandicarboxylate): an in situ simultaneous SAXS-WAXS study, Polym. Eng. Sci. 59 (2019) 1667–1677, https://doi.org/10.1002/pen.25165.
[18] G. Stoclet, G. Gobius du Sart, B. Yeniad, S. de Vos, J.M. Lefebvre, Isothermal crystallization and structural characterization of poly(ethylene-2,5-furanoate), Polymer 72 (2015) 165–176, https://doi.org/10.1016/j.polymer.2015.07.014.
[19] M. Matos, A.F. Sousa, A.J.D. Silvestre, Improving the thermal properties of poly (2,5-furandicarboxylate)s using cyclohexylene moieties: a comparative study, Macromol. Chem. Phys. 218 (2017), https://doi.org/10.1002/macp.201600492.
[20] A.F. Sousa, C. Vilela, A.C. Fonseca, M. Matos, C.S.R. Freire, G.-J.M. Gruter, J.F. J. Coelho, A.J.D. Silvestre, Biobased polyesters and other polymers from 2,5-furandicarboxylic acid: a tribute to furan excellency, Polym. Chem. 6 (2015) 5961–5983, https://doi.org/10.1039/C5PY00686D.
[21] A. Codou, M. Moncel, J.G. van Berkel, N. Guigo, N. Sbirrazzuoli, Glass transition dynamics and cooperativity length of poly(ethylene 2,5-furandicarboxylate) compared to poly(ethylene terephthalate), Phys. Chem. Chem. Phys. 18 (2016) 16647–16658, https://doi.org/10.1039/C6CP01227B.
[22] A. Codou, N. Guigo, J. van Berkel, E. de Jong, N. Sbirrazzuoli, Non-isothermal crystallization kinetics of biobased poly(ethylene 2,5-furandicarboxylate) synthesized via the direct esterification process, Macromol. Chem. Phys. 215 (2014) 2065–2074, https://doi.org/10.1002/macp.201400316.
[23] N. Guigo, J. van Berkel, E. de Jong, N. Sbirrazzuoli, Modelling the non-isothermal crystallization of polymers: application to poly(ethylene 2,5-furandicarboxylate), Thermochim. Acta 650 (2017) 66–75, https://doi.org/10.1016/j.tca.2017.02.008.
[24] J.G. van Berkel, N. Guigo, H.A. Visser, N. Sbirrazzuoli, Chain structure and molecular weight dependent mechanics of poly(ethylene 2,5-furandicarboxylate) compared to poly(ethylene terephthalate), Macromolecules 51 (2018) 8539–8549, https://doi.org/10.1021/acs.macromol.8b01831.
[25] L. Martino, N. Guigo, J.G. Van Berkel, J.J. Kolstad, N. Sbirrazzuoli, Nucleation and self-nucleation of bio-based poly(ethylene 2,5-furandicarboxylate) probed by fast scanning calorimetry, Macromol. Mater. Eng. 301 (2016) 586–596, https://doi.org/10.1002/mame.201500418.
[26] J.G. van Berkel, N. Guigo, J.J. Kolstad, L. Sipos, B. Wang, M.A. Dam, N. Sbirrazzuoli, Isothermal crystallization kinetics of poly (ethylene 2,5-furandicarboxylate), Macromol. Mater. Eng. 300 (2015) 466–474, https://doi.org/10.1002/mame.201400376.
[27] S.K. Burgess, R.M. Kriegel, W.J. Koros, Carbon dioxide sorption and transport in amorphous poly(ethylene furanoate), Macromolecules 48 (2015) 2184–2193, https://doi.org/10.1021/acs.macromol.5b00333.
[28] S.K. Burgess, G.B. Wenz, R.M. Kriegel, W.J. Koros, Penetrant transport in semicrystalline poly(ethylene furanoate), Polymer 98 (2016) 305–310, https://doi.org/10.1016/j.polymer.2016.06.046.
[29] S.K. Burgess, C.R. Mubarak, R.M. Kriegel, W.J. Koros, Physical aging in amorphous poly(ethylene furanoate): enthalpic recovery, density, and oxygen transport considerations, J. Polym. Sci. B Polym. Phys. 53 (2015) 389–399, https://doi.org/10.1002/polb.23648.
[30] S.K. Burgess, O. Karvan, J.R. Johnson, R.M. Kriegel, W.J. Koros, Oxygen sorption and transport in amorphous poly(ethylene furanoate), Polymer 55 (2014) 4748–4756, https://doi.org/10.1016/j.polymer.2014.07.041.
[31] S.K. Burgess, D.S. Mikkilineni, D.B. Yu, D.J. Kim, C.R. Mubarak, R.M. Kriegel, W. J. Koros, Water sorption in poly(ethylene furanoate) compared to poly(ethylene terephthalate). Part 2: kinetic sorption, Polymer 55 (2014) 6870–6882, https://doi.org/10.1016/j.polymer.2014.10.065.
[32] S.K. Burgess, D.S. Mikkilineni, D.B. Yu, D.J. Kim, C.R. Mubarak, R.M. Kriegel, W. J. Koros, Water sorption in poly(ethylene furanoate) compared to poly(ethylene terephthalate). Part 1: equilibrium sorption, Polymer 55 (2014) 6861–6869, https://doi.org/10.1016/j.polymer.2014.10.047.
[33] F.W. Gomes, R.C. Lima, C.R. Piombini, J.F. Sinfitele, F.G. de Souza, P.L. A. Coutinho, J.C. Pinto, Comparative analyses of poly(ethylene 2,5-furandicarboxylate) – PEF – and poly(ethylene terephthalate) – PET – resins and production processes, Macromol. Symp. 381 (2018), https://doi.org/10.1002/masy.201800129.
[34] C. Millot, L.A. Fillot, O. Lame, P. Sotta, R. Seguela, Assessment of polyamide-6 crystallinity by DSC: temperature dependence of the melting enthalpy, J. Therm. Anal. Calorim. 122 (2015) 307–314, https://doi.org/10.1007/S10973-015-4670-5/FIGURES/4.
[35] C.F. Araujo, M.M. Nolasco, P.J.A. Ribeiro-Claro, S. Rudić, A.J.D. Silvestre, P. D. Vaz, A.F. Sousa, Inside PEF: chain conformation and dynamics in crystalline and amorphous domains, Macromolecules 51 (2018) 3515–3526, https://doi.org/10.1021/acs.macromol.8b00192.
[36] A.F. Sousa, R. Patricio, Z. Terzopoulou, D.N. Bikiaris, T. Stern, J. Wenger, K. Loos, N. Lotti, V. Siracusa, A. Szymczyk, S. Paszkiewicz, K.S. Triantafyllidis, A. Zamboulis, M.S. Nikolic, P. Spasojevic, S. Thiyagarajan, D.S. van Es, N. Guigo, Recommandations for replacing PET on packaging, fiber, and film materials with biobased counterparts, Green Chem. 23 (2021) 8795–8820, https://doi.org/10.1039/D1GC02082J.
[37] A.J.J.E. Eerhart, A.P.C. Faaij, M.K. Patel, Replacing fossil based PET with biobased PEF; Process analysis, energy and GHG balance, Energy Environ. Sci. 5 (2012) 6407–6422, https://doi.org/10.1039/c2ee02480b.
[38] E. de Jong, H. Roy, A. Visser, A.S. Dias, C. Harvey, G.-J.M. Gruter, The road to bring FDCA and PEF to the market, Polymers 14 (2022) 943, https://doi.org/10.3390/POLYM14050943, 943 14 (2022.
[39] K. Loos, R. Zhang, I. Pereira, B. Agostinho, H. Hu, D. Maniar, N. Sbirrazzuoli, A.J. D. Silvestre, N. Guigo, A.F. Sousa, A perspective on PEF synthesis, properties, and end-life, Front. Chem. 8 (2020) 585, https://doi.org/10.3389/fchem.2020.00585.
[40] Frontiers | A Perspective on PEF Synthesis, Properties, and End-Life | Chemistry, (n.d.). https://www.frontiersin.org/articles/10.3389/fchem.2020.00585/full#B28 (accessed August 5, 2020).
[41] A.F. Sousa, R. Patrício, Z. Terzopoulou, D.N. Bikiaris, T. Stern, J. Wenger, K. Loos, N. Lotti, V. Siracusa, A. Szymczyk, S. Paszkiewicz, K.S. Triantafyllidis, A. Zamboulis, M.S. Nikolic, P. Spasojevic, S. Thiyagarajan, D.S. Van Es, N. Guigo, Recommendations for replacing PET on packaging, fiber, and film materials with biobased counterparts, Green Chem. 23 (2021) 8795–8820, https://doi.org/10.1039/D1GC02082J.
[42] E. Forestier, C. Combeaud, N. Guigo, N. Sbirrazzuoli, Mechanical behaviour and induced microstructural development upon simultaneous and balanced biaxial stretching of poly(ethylene furandicarboxylate), PEF, Polymers 15 (2023) 661, https://doi.org/10.3390/POLYM15030661, 661 15 (2023.
[43] E. Forestier, N. Guigo, C. Combeaud, N. Billon, N. Sbirrazzuoli, Conformational change analysis of poly(ethylene 2,5-furandicarboxylate) and poly(ethylene terephthalate) under uniaxial stretching, Macromolecules (2020), https://doi.org/10.1021/acs.macromol.0c00691.
[44] G. Stoclet, S. Xu, V. Gaucher, J.F. Tahon, S. van Berkel, A. Arias, C. Rogeret, R. Nourichard, S. de Vos, Influence of the molecular weight on mechanical behavior and associated strain-induced structural evolution of Poly(ethylene 2,5-furandicarboxylate) upon biaxial stretching, Polymer 217 (2021) 123441, https://doi.org/10.1016/j.polymer.2021.123441.
[45] Y. Mao, R.M. Kriegel, D.G. Bucknall, The crystal structure of poly(ethylene furanoate), Polymer 102 (2016) 308–314, https://doi.org/10.1016/j.polymer.2016.08.052.
[46] Y. Mao, D.G. Bucknall, R.M. Kriegel, Synchrotron X-ray scattering study on amorphous poly(ethylene furanoate) under uniaxial deformation, Polymer 139 (2018) 60–67, https://doi.org/10.1016/j.polymer.2018.01.062.
[47] C.R. Desper, R.S. Stein, Measurement of Pole figures and orientation functions for polyethylene films prepared by unidirectional and oriented crystallization, J. Appl. Phys. 37 (1966) 3990–4002, https://doi.org/10.1063/1.1707966.
[48] Z.W. Wilchinsky, Orientation in cold-rolled polypropylene, J. Appl. Polym. Sci. 7 (1963) 923–933, https://doi.org/10.1002/APP.1963.070070311.